Astron. Astrophys. 320, 147–158 (1997)

ASTRONOMY
AND
ASTROPHYSICS

ASCA and EUVE observations of II Pegasi: flaring and quiescent coronal emission

R. Mewe[1], **J.S. Kaastra**[1], **G.H.J. van den Oord**[2], **J. Vink**[1], **and Y. Tawara**[3]

[1] SRON Laboratory for Space Research, Sorbonnelaan 2, 3584 CA Utrecht, The Netherlands
[2] Sterrekundig Instituut Utrecht, P.O. Box 80000, 3508 TA Utrecht, The Netherlands
[3] Department of Physics, Nagoya University, Chikusa-ku, Nagoya 464, Japan

Received 8 July 1996 / Accepted 17 September 1996

Abstract. We have analyzed X-ray and EUV spectra of both the quiescent and flaring state of II Peg, obtained from observations with ASCA and EUVE. Coronal temperature structure and abundances have been derived from multi-temperature and differential emission measure (DEM) analyses of the spectra. The abundances are non-solar; in the case of ASCA for most elements (O, Ne, Mg, Si, S, Ar, Ca, Ni) we obtain abundances that are consistent with about 1/2-1/5 of the solar photospheric abundances of Anders and Grevesse (1989), but the Fe abundance is even lower, i.e. 0.1 $\times$ solar. The multi-T and DEM fitting analysis shows that the quiescent EUVE and ASCA spectra can be described by two temperature components: 4 and 10 MK (EUVE), 10 and 20 MK (ASCA). The two flares detected by EUVE and ASCA show peak temperatures of 20 and $\gtrsim$ 35 MK, respectively. The latter flare has a total energy (0.1-10 keV) of 2.7 10^{34} erg, a peak luminosity of 2.6 10^{30} erg/s. There is evidence for an increase of a factor $\sim$ 4 of the iron abundance during the rise phase of the flare. Application of a cooling model yields a loop height of about 8 10^{10} cm and a plasma density of 8 10^{10} cm^{-3}.

Key words: stars: coronae – activity – late-type – flare – abundances – II Peg – ultraviolet: stars – X-rays: stars

1. Introduction

II Peg (=HD 224085 = BD +27 4642 = HIC 117915 = SAO 91578) is a single-line spectroscopic binary with a K2IV-V primary. No trace of the companion has ever been found, in either the photospheric or the chromospheric spectrum, leading to the conclusion that it is a faint object, possibly a very late-type M dwarf (Byrne et al. 1995). The orbital period is approximately 6.7 days. The distance of the binary derived from a weighted parallax of 0.34″ (Jenkins 1963, see also Vogt 1981) is 29.4 pc. Originally the star was classified as a BY Dra-type variable based on the observed wave-like photometrical variability which was attributed to cool surface spots. Rucinski (1977) showed that the object is probably an RS CVn-variable. The stellar radius of the primary is $R_* = 2.8R_\odot$ and the binary separation is $a = 4.9R_\odot$ (for an inclination $\approx 90^0$) (Strassmeier et al. 1988).

II Peg is a magnetically active binary which has been extensively studied at optical, UV (Rodonò et al. 1986, 1987; Andrews et al. 1988; Byrne et al. 1989; Doyle et al. 1989a) and X-ray wavelengths (Swank et al. 1981; Tagliaferri et al. 1991; Doyle et al. 1992b) while a limited number of radio observations are available (see overview in van den Oord and De Bruyn 1994).

II Peg is one of the most interesting RS CVn-type stars to study flare activity. Strong flares have been seen in the radio, optical, UV and X-ray bands. This flare activity shows up predominantly in the UV and X-rays; in fact, flares have been seen in all the IUE runs of 1981, 1983, 1985 and 1986. UV flares can reach energies of up to a few times 10^{36} ergs (Doyle et al. 1989b). Mathoudiakis et al. (1992) report an optical U-band flare frequency of $\sim$ 0.15 hr^{-1}, but Byrne et al. (1994) could not confirm such a high rate (in fact they detected no U-band flaring down to very low limits in a 32 hrs period).

In X-rays two strong flares have been seen with EXOSAT and with GINGA, with an energy release of $>$ 2 10^{35} erg in both cases. The flare detected by EXOSAT in the 0.05-7 keV energy band, lasted for more than one day, with a rise time of $\sim$ 3 hours, the peak phase lasted at least 2 hours and then there was a long decay, which however was not continuously observed by EXOSAT due to perigee passage. The quiescent value was reached again about two days after the flare occurred (Tagliaferri et al. 1991). The strong GINGA flare was observed only partially during the decay phase, but still was so intense that GINGA was able to detect it up to 15 keV (Doyle et al. 1992a). EINSTEIN, EXOSAT and GINGA have detected quiescent coronal X-ray emission. From an EINSTEIN survey of RS CVn binaries Swank et al. (1981) concluded that the spectra of these

Send offprint requests to: R. Mewe

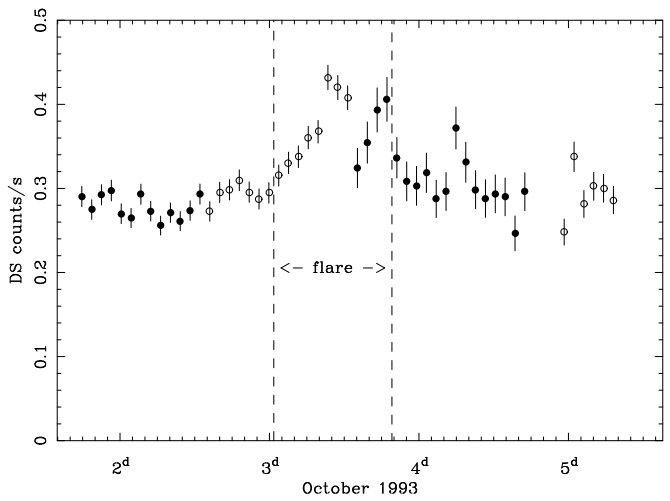

Fig. 1. Corrected light curve of II Peg observations with the EUVE Deep Sky instrument ($\sim$ 80-200 Å). The different symbols indicate the four periods.

binaries in the 0.5-4 keV range can be fitted by two emission components with temperatures of 4-8 MK and 20-100 MK and emission measures varying in the ratio 0.1-4 where the cooler component is roughly constant with an emission measure of $\sim 3\ 10^{53}$ cm^{-3}. A similar result was found from a series of EXOSAT observations of II Peg using the ME (1-6 keV) and the CMA (0.05-2 keV). The temperatures found are: $T_1 \sim$ 3.5-8 MK and $T_2 \sim$ 17-30 MK (Tagliaferri et al. 1991). Of special interest is the detection by GINGA of a power-law tail up to 18 keV in the quiescent spectrum of II Peg (Doyle et al. 1992b). These authors showed that the power-law cannot be interpreted as non-thermal emission because of the energy requirements, but can be explained in terms of a differential emission measure distribution of the form $\propto T^{-3/2}$, which implies a considerable fraction of hot ($\sim$ 100 MK) coronal plasma. Simultaneous radio observations (VLA) at 3.6, 6 and 20 cm could be interpreted as gyro-synchrotron emission from this thermal plasma (Doyle et al. 1992b).

With the scanning telescopes on EUVE II Peg has been observed by Patterer et al. (1993) during its quiescent state and also during a flare with characteristics similar to previously observed flares on II Peg.

In Sect. 2 we present the spectral extraction procedures; in Sect. 3 the spectral fitting procedure is shortly described; in Sect. 4 the results from the multi-temperature and DEM fitting methods are described. In Sect. 5 we model the flare decay to determine the physical parameters (height, volume, and density) of the flare region, and in Sect. 6 we discuss the results.

2. Observations

2.1. EUVE observations

II Peg was observed by the Extreme UltraViolet Explorer (EUVE) in 1993 from October 1, 13^h55 UT to October 5, 8^h48 UT. Data were obtained with the Deep Sky (DS) instrument as well as with the SW, MW and LW spectrometers.

2.1.1. The light curve

The DS instrument of EUVE is the most sensitive to detect variability. We have constructed the background-subtracted light curve for II Peg. Unfortunately, the observations were performed with II Peg close to the position of the dead spot on the DS detector, which was caused by damage during an observation of HZ 43 in January 1993. During the present observation, the pointing changed 4 times slightly, causing the image of II Peg to overlap differently over the dead spot. We have corrected for this by scaling the DS count rates with the average DS-to-SW ratio during the 4 periods of stable pointing (the count rates in the 4 periods have thus been multiplied by 1.00, 1.00, 3.25 and 1.80, respectively). The statistical uncertainty in these scaling factors is typically 6-10 %.

The light curve is shown in Fig. 1. We have plotted the average count rate over one orbit (about 5690 s). Effectively, we obtained only data during a continuous time interval of 36 % of each orbit. Note the flare occurring on October 3 which lasted for about 18 hours.

2.1.2. Spectral extraction

The spectra were extracted from the spectral images using the EUVEXTRACT program of the Center for EUV Astrophysics (CEA). In order to account for systematic variations in the effective area due to fixed-pattern noise, we added a systematic error of 4 % of the source flux to the SW data, and of 8 % to the MW and LW data (cf. Figs. 5-3 and 5-4 of the EUVE data product guide). Inspection of the background showed that there is no need to include a systematic error in the background.

We divided the data into two parts: a quiescent spectrum, before and after the flare as indicated in Fig. 1, and a flare spectrum. The net exposure time was about 87 ks for the quiescent spectrum and 24 ks for the flare spectrum.

We have omitted the spectrum above 290 Å from our analysis. This part contained as the only significant feature the 304 Å line of He II, which is known to be optically thick, and probably caused by a very cool plasma component that gives no other significant contributions in the wavelength range below 290 Å. At 284.15 Å there is a weak Fe XV line visible in the spectrum, and consequently we kept the whole region below 290 Å in our spectra.

2.2. ASCA observations

The Advanced Satellite for Cosmology and Astrophysics (ASCA) observed II Peg in 1994 from December 18, 20^h32 UT to December 19, 21^h40 UT. Data were obtained with the SIS detectors as well as with the GIS detectors. A flare - with a rise time of $\lesssim$ 1 hour and a decay time of $\sim$ 3 hours - was observed in the SIS data starting at about December 19, 13^h00 UT and

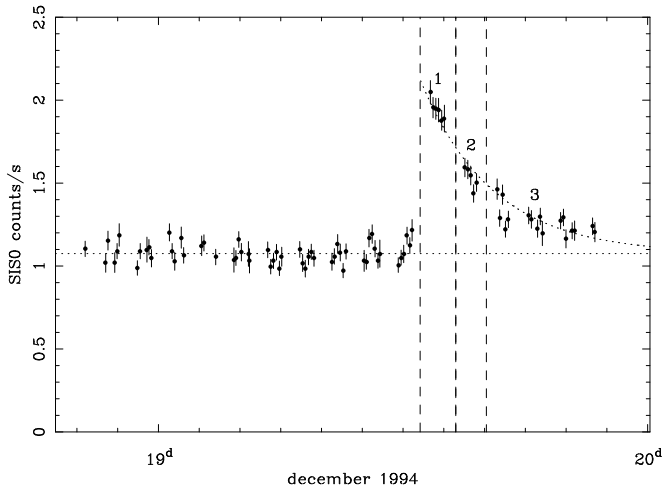

Fig. 2. Light curve of II Peg observations with the ASCA SIS0 detector. The dotted lines are fits to the data. For the analysis of the flare the observations are divided into 3 parts as indicated in the figure.

lasting until the end of the observation for about 8 hours (see the light curve in Fig. 2).

2.2.1. Spectral extraction

The spectra were extracted from the spectral images using the NASA software package FTOOLS/XSELECT. We summed the signals from both SIS0 and SIS1 detectors and in order to account for systematic uncertainties and differences in the calibration of the effective areas of the two detectors, we added a systematic error of 5 % of the source flux to the data and deleted data points below about 0.5 keV and above about 10 keV. The SIS spectra were rebinned into 155 energy bins to ensure a sufficient signal-to-noise ratio S/N per bin, i.e. N $\gtrsim$ 20 cts/bin. The source signal was determined in a circle of about 6.5′ diameter and the background was determined using the background event lists provided by NASA HEASARC. However, we noticed a significant excess flux in the background-subtracted spectrum above about 8 keV (cf. Fig. 5) which is also seen in other SIS observations of coronal sources (e.g., Kaastra et al. 1996b, Mewe et al. 1996). In order to investigate whether this could be due to the background subtraction we also determined the background in a $\sim$ 6.5′ circle in the detector image opposite to the source, but this did not remove the excess flux at high energies.

We divided the SIS (S0 + S1) data into four parts: the quiescent spectrum before the flare and the flare spectrum subdivided into three parts (see Fig. 2). The net exposure time for the quiescent period was about 48 ks and for the total flare period about 22 ks. The GIS (GIS2 + GIS3) data covered only a part of the quiet period with a net exposure time of about 11 ks. No data were available during the flare. We deleted the data below 0.6 keV and above 6 keV and rebinned the spectrum into 126 energy bins to get sufficient statistics.

3. Spectral fitting

For our spectral analysis, we have used the SPEX software package (Kaastra et al. 1996a). This package contains models for the calculation of spectra from optically thin plasmas in collisional ionization equilibrium (CIE) (Mewe et al. 1985, 1986; Kaastra and Mewe 1993). Recently the calculations for the Fe-L complexes have been updated using results from the HULLAC code (Liedahl et al. 1995) and various other improvements have been made (cf. Mewe et al. 1995). We express abundances relative to the solar photospheric values taken from Anders & Grevesse (1989). For the ionization balance we use Arnaud and Rothenflug (1985) for all elements except iron, for which we use the update of Arnaud and Raymond (1992). Emission measures are defined here as $EM = \int n_{\rm e} n_{\rm H} {\rm d}V$, where $n_{\rm e}$ is the electron density, $n_{\rm H}$ is the hydrogen density and V the emitting volume. Galactic absorption is taken into account using the model of Morrison and McCammon (1983) for the ASCA data and that of Rumph et al. (1994) for the EUVE data.

4. Results

4.1. EUVE data

4.1.1. Multi-temperature fits

a. Quiescent spectrum

The EUVE spectrum of the quiescent phases was fitted with two components in collisional ionization equilibrium. We adopted the same abundances for both components. Moreover, we assumed initially that the abundances of all heavy elements (from C to Ni) are equal to the iron abundance in order to constrain the number of free parameters.

It appeared in our fit that the interstellar hydrogen column density is not well constrained: we found a best-fit value of $N_H = 5.0^{+1.8}_{-3.4}\ 10^{18}$ cm^{-2}. This value is close to the value that can be derived from the distance to the object using the average interstellar hydrogen density of 0.07 cm^{-3} from Paresce (1984). Consequently, we fixed this parameter to 5 10^{18} cm^{-2} in all our subsequent fits.

We have checked for the most important elements in this EUVE spectrum (O, Ne and Ni) whether their abundances differ significantly from the iron abundance. Only for neon this appears to be the case: we find a Ne/Fe abundance ratio of 1.9$\pm$0.9. Consequently, we have adopted in all our fits a constant Ne/Fe abundance ratio of 1.9.

We find best-fit temperatures of $T_1 = 3.6 \pm 0.3$ MK and $T_2 = 10.4^{+2.3}_{-0.9}$ MK for the cool and hot component, respectively, with corresponding emission measures $EM_1 = 2.21 \pm 0.24\ 10^{53}$ cm^{-3} and $EM_2 = 0.69 \pm 0.22\ 10^{53}$ cm^{-3}. The iron abundance is 0.16$\pm$0.05 $\times$ solar. The fit is acceptable: χ^2 = 431 for 414 degrees of freedom (dof). The best-fit spectrum is compared to the observations in Fig. 3.

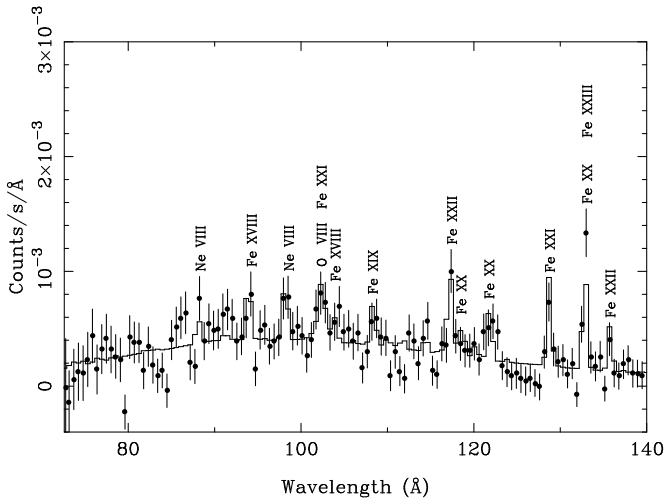

Fig. 3. Observed and fitted EUVE SW quiescent spectrum of II Peg for a 2-T fit with non-solar abundances. Only the 72-140 Å part is shown because the remaining spectrum contains mainly continuum. Error bars indicate $\pm 1\sigma$ errors. Some prominent lines are indicated by the ions from which they originate.

b. Flare spectrum

Due to the shorter exposure time the statistics of the flare spectrum is not as good as that of the quiescent spectrum. Therefore we fixed the abundances to the values found or used in the analysis of the quiescent spectrum. A two-temperature fit showed for the cool component essentially the same parameters as for the quiescent spectrum. Therefore in the subsequent analysis we fixed the emission measure and temperature of the cool component to the corresponding parameters of the quiescent spectrum. Our best fit (χ^2 = 465 for 414 dof) shows that the hot component has increased considerably both in emission measure $2.3\pm0.5\ 10^{53}$ cm^{-3} - an increase of a factor 3.6 - and in temperature 19.6 ± 2.3 MK - an increase of a factor 1.9.

Does the flare arise as a change in the hot component, or is it a new component previously not present in the source? In order to test this, we have tried a model consisting of the 2 quiescent components plus an extra, third flare component. We found for this flare component an emission measure of $1.4\pm0.5\ 10^{53}$ cm^{-3} and a temperature of 23^{+13}_{-4} MK, however with a χ^2 increase of 11 compared to the previous two-temperature fit. We conclude that the inclusion of a third component does not improve the fit and that it is likely that the flare is related to the hot component derived from the quiescent spectrum.

We remark that part of the rise in the emission measure could be due to an increase of the iron abundance. The iron abundance follows mainly from the observed line-to-continuum ratios for the different Fe lines. If during the flare the Fe abundance increases by say a factor f and the emission measure remains unchanged, the strength of the Fe lines increases with this factor f. Because we fixed the elemental abundances on the pre-flare values, an observed increase of the Fe line intensities is attributed to an increase by a factor of f of the emission measure. The observed value $f \simeq 3.6$ is close to the abundance increase of about 4 found during the ASCA flare (cf. Sect. 4.2.1.b). It is however likely that variations of both the emission measure and the Fe abundance occur which are difficult to disentangle because the S/N is rather poor and the spectrum contains an unchanged quiescent component. Based on the light curve (Fig. 1) we estimate that the possible variation of the Fe abundance is at most about 30%.

4.1.2. Differential emission measure (DEM) analysis

We also applied a differential emission measure (DEM) analysis to the present data. One of the most powerful and reliable methods to analyze discrete temperature structures is the Chebyshev polynomial method (see e.g., Kaastra et al., 1996b), which we have applied here. We fixed the abundances and N_H to the values found in our two-temperature fit.

We have used a temperature grid between 0.1-10 keV (it appeared in our fits that there is essentially no emission from the 0.01-0.1 keV range) with a spacing of 0.067 in log T to evaluate the spectral components.

For the quiescent spectrum we find essentially the bimodal distribution that was also found from our two-temperature fit. The emission measures are consistent with those of the two-temperature fit. Also the χ^2 is similar: 423 for Chebyshev polynomials up to N = 7 (412 dof).

The temperature distribution of the flare spectrum is also consistent with the relevant two-temperature fit. We get χ^2 = 465 for Chebyshev polynomials up to N = 7 (412 dof).

4.2. ASCA data

4.2.1. Multi-temperature fits

a. Quiescent spectrum

The ASCA SIS spectrum of the quiescent phase was fitted with two components in collisional equilibrium using for the interstellar column density the best-fit value of $5\ 10^{18}$ cm^{-2} as obtained from the EUVE fits. However, the ASCA fits are not sensitive to the precise value of this parameter. Fits with solar abundances are very poor: χ^2 = 1375 for 151 dof (cf. Fig. 4). Many features (e.g, Fe L & K) are not fitted at all! It is clear that we have to vary the abundances of those elements that produce detectable line features in the ASCA spectrum.

Elements for which relatively strong, isolated lines are present in the spectrum yield the most reliable abundances (e.g., Fe, S, Si, Mg, Ne, and O) of which the Fe abundance is most accurately determined by the Fe L-shell $\sim$ 1 keV complex and sometimes also the 6.7 keV Fe K-shell feature (in the flare). The abundances of Si and S are predominantly determined from the He- and H-like line complexes at $\sim$ 1.9 and $\sim$ 2.5 keV, respectively. The O abundance is mainly derived from the 0.65 keV Lyman α line, which is however partly blended by the Fe L complex. The Mg abundance is essentially based on the He- and H-like line complex at $\sim$ 1.4 keV. The Ne abundance is de-

Table 1. Temperatures T and emission measures EM for the quiescent (Q) and the flare (Fl#)[1] phases of II Peg from the ASCA SIS data

Phase	T_1 (MK)	EM_1 (10^{53} cm^{-3})	T_2 (MK)	EM_2 (10^{53} cm^{-3})	Fe abundance[2]	χ^2	dof
Q	9.9 ± 0.6	1.83 ± 0.34	21.6 ± 1.9	1.29 ± 0.26	0.094±0.017	198	142
Fl1	36.2 ± 2.0	2.00 ± 0.07			0.382±0.094	151	127
FL2	28.0 ± 3.4	1.10 ± 0.10			0.32±0.19	80	70
FL3	25.7 ± 3.0	0.57 ± 0.05			< 0.21	129	97

[1] Flare emission in time interval nr. # (cf. Fig. 2), corrected for the quiescent emission.
[2] Fe abundance was varied, and for Q 8 other abundances were varied or for FL kept fixed to the values in Table 2.

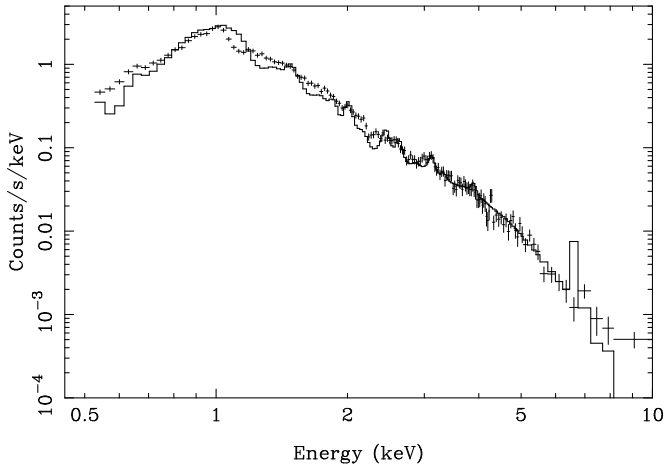

Fig. 4. Observed and fitted ASCA SIS quiescent spectrum of II Peg for a 2-T fit with solar abundances. Error bars indicate $\pm 1\sigma$ errors.

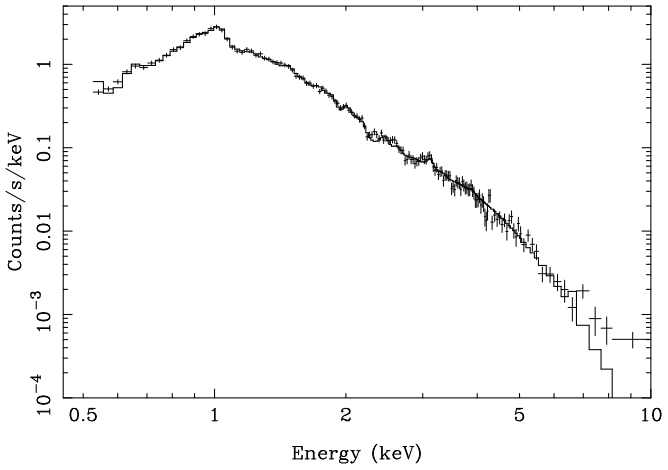

Fig. 5. Observed and fitted ASCA SIS quiescent spectrum of II Peg for a 2-T fit with non-solar abundances (Table 2). Error bars indicate $\pm 1\sigma$ errors.

rived from the 0.92 keV Ne IX and 1.02 keV Ne X lines, which however are just in the middle of the Fe L feature.

We have varied the abundances of the 9 most important elements, but we have forced the abundances to be the same for the two temperature components. The N abundance was fixed at a low value of 0.01 to compensate for the calibration errors near 0.5 keV and the abundances of the other elements (He, C, Na and Al) were fixed at solar values as our measurements are not sensitive enough to put useful constraints on these abundances.

The best-fit temperatures and the corresponding emission measures of the cool and hot component are given in Table 1. Addition of a third component does not improve the fit significantly (decrease of 8 in χ^2). The best-fit abundances which are significantly below solar - especially the Fe abundance - are given with their statistical 1σ uncertainties in Table 2. The spectrum and the best-fit model are shown in Fig. 5 and the fit residuals between 2-5 keV in Fig. 6. The fit is much better but still not acceptable: χ^2 = 198 for 142 dof. This is mainly caused by the poor fit to the spectrum below 0.6 keV and above 8 keV (where the calibration uncertainties are quite large) and by several strange features in the data around 2.5 keV (S K & Lyα lines) and 4 keV (Ca K & Lyα) for which we have no explanation.

The quiescent GIS spectrum was fitted with two temperature components (an additional component does not improve the fit) and using the abundances obtained earlier (Table 2). We obtain χ^2 = 143 for 122 dof with values for temperatures and emission measures consistent, within the statistical errors, with the results for the SIS spectrum.

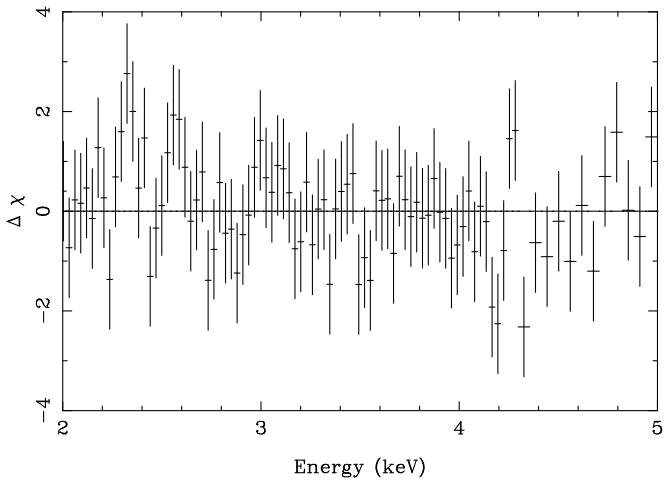

Fig. 6. Fit residuals of the ASCA SIS quiescent spectrum of II Peg using a 2-temperature fit method with non-solar abundances (Table 2). Error bars indicate $\pm 1\sigma$ errors.

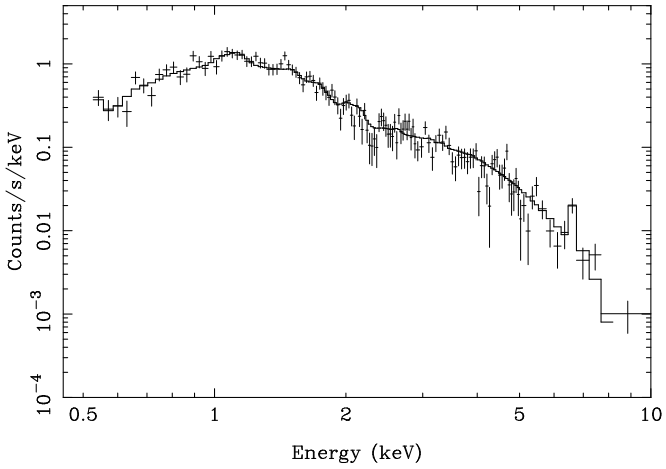

Fig. 7. Observed and fitted ASCA SIS flare-only peak spectrum (FL1) of II Peg for a 1-T fit with the abundances from Table 2, except for the Fe abundance which is given in Table 1. Error bars indicate $\pm 1\sigma$ errors.

Table 2. Abundances[1] for the quiescent corona of II Peg relative to solar photospheric values of Anders & Grevesse (1989)[2]

Element	Abundance	Element	Abundance
O	0.30 ± 0.08	Ar	0.34 ± 0.19
Ne	0.63 ± 0.18	Ca	< 0.5
Mg	0.16 ± 0.07	Fe	0.094 ± 0.017
Si	0.20 ± 0.04	Ni	0.35 ± 0.26
S	0.17 ± 0.05		

[1] The N abundance was fixed to a value of 0.01 × solar.
[2] In logarithmic units, with $\log_{10}$H=12.00: O,8.93; Ne,8.09; Mg,7.58; Si,7.55; S,7.21; Ar, 6.56; Ca, 6.36; Fe,7.67; Ni,6.25.

b. Flare spectrum

The first part of the ASCA light curve (cf. Fig. 2) is very constant, indicating the quiescent emission regions to be constant over the observation both in intensity and location. Therefore we adopt this part as the quiescent pre-flare emission and assume that the flare originates from a region which differs - at least partly - from the region that produces the quiescent radiation. To obtain the flare-only spectra we have subtracted the quiescent pre-flare spectrum from the flare spectrum. We have made 1- and 2-T fits to these flare-only spectra. Due to the shorter exposure time and the substraction of the quiescent spectrum the statistics of the the flare spectra are not as good as that of the quiescent spectrum. Therefore we have rebinned the spectra (FL1, 2 & 3 into 130, 73, and 100 bins, respectively), in order to obtain a sufficient S/N ratio, i.e. N $\gtrsim$ 10 cts per bin.

The best-fit temperatures and emission measures are given in Table 1 and for the flare peak FL1 we give in Fig. 7 the observed and fitted SIS spectrum. We notice the appearance of the Fe K feature at 6.7 keV associated with the higher temperature. The results for the peak flare spectrum are consistent with a 1-T model. Though the following decay phases are slightly better fitted with 2-T models, we present the 1-T fit results as it turns out that one of the two components has a significance of only $\sim 1\sigma$.

From the results of the fits we derive a peak luminosity of L_X(0.1-10.0 keV) $\simeq 2.6\ 10^{30}$ erg/s, comparable to the quiescent value of $2.8\ 10^{30}$ erg/s, and by integrating over the total flare duration a total flare energy during the decay of $E_{\rm tot} \simeq 2.7\ 10^{34}$ erg.

The statistics of the flare spectra does not allow to determine all element abundances as we did for the quiescent spectrum. However, variation of the metal (i.e., iron) abundance gives for the flare peak FL1 a significantly better fit than for the case in which all abundances were fixed to the quiescent values (χ^2 =151 (127 dof) *vs.* χ^2 =173 (128 dof), respectively). During the rise of the flare the iron abundance has increased by a factor of 4 compared to the quiescent value with a significance at the 3σ level, i.e. Fe 0.382 ± 0.094 compared to 0.094 in the quiescent phase (cf. Table 1). To investigate whether also other element abundances vary during the rise of the flare we varied in addition to the iron abundance the other 8 abundances coupled to the nickel abundance. The fit did not improve (same χ^2) and the coupled abundances were allowed to vary in the $\pm 1\sigma$ range by a factor 1/8 to 2, hence they are in fact undetermined and only the iron abundance is decisive.

For the later phases in the flare also the iron abundance is less well determined and becomes at the end of the flare equal to the corresponding quiescent value within the statistical uncertainty (cf. Table 1).

4.2.2. DEM analysis

Initially we used a temperature grid between 0.1-10 keV but as it appeared in our fits that essentially no emission is present in the 0.1-0.5 keV range, we have used a temperature grid between 0.5-10 keV with a spacing of 0.05 in log T. We adopt the abundances

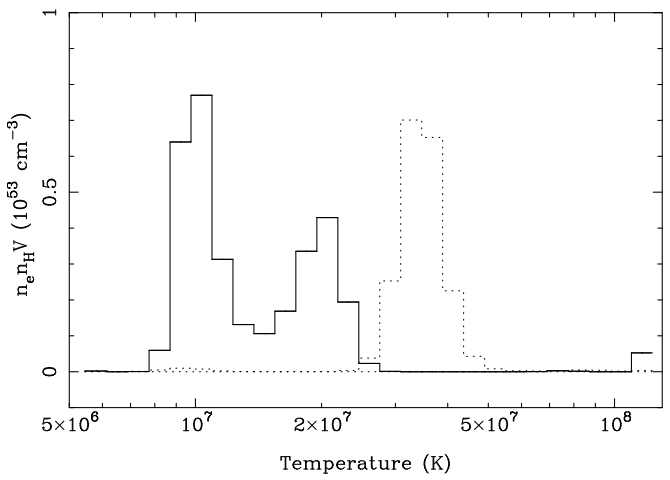

Fig. 8. The DEM for the quiescent SIS spectrum using the polynomial method with non-solar abundances (Table 2) (solid line) and for the flare peak FL1 (dotted line) with abundances from Table 2, except for the Fe abundance which was taken from Table 1.

of Table 2, except for the Fe abundance during the flare for which we take the values from Table 1.

For the quiescent SIS spectrum we find essentially the bimodal temperature distribution that was also found from our two-temperature fit with comparable emission measures. Also the χ^2 is similar: χ^2 = 196 (121 dof) for a fit with Chebyshev polynomials up to N = 9 (see Fig. 8).

The temperature distributions of the flare spectra are consistent with the previously obtained one-temperature fits and we get comparable χ^2's, e.g., for the flare peak, χ^2 = 159 (120 dof) for Chebyshev polynomials with N = 10 (cf. Fig. 8).

5. Flare modeling

By studying the decay of a flare we can estimate from the cooling time the volume V and size (loop height H) of the flare region and, together with the observed emission measure, also the plasma (electron) density n_e. In this section we consider the flare observed with ASCA.

A general treatment of the decay of a flare was proposed by van den Oord et al. 1988 (hereafter VMB88). A more complete description can be found in van den Oord and Mewe 1989 (VM89, Sect. 3.1). In the model it is assumed that the flare light curve and the temperature decrease exponentially with decay times $\tau_{\rm d}$ and $\tau_{\rm T}$, respectively. The decrease of the thermal energy of the cooling plasma is caused by radiative and conductive losses. Under the assumption of an exponential time dependence, the characteristic time scale $\tau_{\rm eff}$ on which the thermal energy decreases can be related to the observed time scales $\tau_{\rm d}$ and $\tau_{\rm T}$ and the time scales for radiative $\tau_{\rm r}$ and conductive losses $\tau_{\rm c}$

$$\frac{1}{\tau_{\rm eff}} = \frac{7/8}{\tau_{\rm T}} + \frac{1}{2\tau_{\rm d}} = \frac{1}{\tau_{\rm r}} + \frac{1}{\tau_{\rm c}}\ . \qquad (1)$$

The time scales for radiative and conductive cooling are defined as

$$\tau_{\rm r} = \frac{3n_e kT}{E_{\rm r}}, \quad \tau_{\rm c} = \frac{3n_e kT}{E_{\rm c}}, \qquad (2)$$

with the volume-averaged radiative (for $T \gtrsim 20$ MK) and conductive losses (in erg cm^{-3} s^{-1}) given by

$$E_{\rm r} = n_e^2 \Psi_0 T^{-\gamma} \simeq 10^{-24.73} n_e^2 T^{0.25},$$
$$E_c = \frac{8f(\Gamma)}{(\Gamma+1)}\kappa_0 \frac{T^{7/2}}{L^2} \simeq 7.0\ 10^{-6} \frac{T^{7/2}}{(\Gamma+1)L^2} f(\Gamma). \qquad (3)$$

In these expressions is T the temperature in K, L the total loop length in cm, n_e the electron density in cm^{-3} , Γ the ratio of the cross-sections at the apex and the base; $f(\Gamma)$ is a correction factor for the conductive flux in tapered loops (Dowdy et al., 1985) which can be approximated as $f(\Gamma) \approx 0.4(\Gamma+1)^{1/2}$. As a first-order approximation we have assumed here a pure hydrogen plasma with $n_e = n_{\rm H}$ and we also neglect the effects of non-solar abundances on the radiative loss function. Assuming that the flare occurs in N identical semi-circular loops with a height $H = L/\pi$ and a base diameter-to-length ratio $\alpha = d/L$, the emission measure EM is related to the flare volume V and the loop height H according to

$$EM = \int n_e n_{\rm H} dV \simeq \int n_e^2 dV \simeq \overline{n_e^2} V$$
$$\simeq \frac{1}{8}\pi^4 \overline{n_e^2} H^3 (1+\Gamma)(N\alpha^2), \qquad (4)$$

where $\overline{n_e^2}$ is the average of the square of the electron density. The factors $(N\alpha^2)$ and $(1+\Gamma)$ express the uncertainty in the detailed flare geometry. The aspect ratio α is typically in the range 0.06-0.2 for active-region loops on the Sun (Golub et al. 1980) and therefore we normalize α to a typical value of 0.1. YOHKOH pictures of the X-ray Sun (Feldman et al. 1994) may indicate that $\Gamma \approx 1$ for the Sun but results for other late-type stars (e.g., Lemen et al. 1989) suggest $\Gamma \gtrsim 10$, so that we allow Γ to vary in the range 1-10.

Substitution of Eqs. (2)-(4) in Eq. (1) gives a cubic equation for $\sqrt{H}$ which has an analytic solution (cf. Eq. (15) of VM89). Because of the assumed exponential behaviour of all quantities it is not important at which moment in the decay phase Eq. (1) is applied. The only restriction is that both the temperature and the emission measure must have started to decrease. We assume that during exposure FL1 the decay phase has started and take $T = T_{\rm FL1}$ = 36 MK and $EM = EM_{\rm FL1} = 2\ 10^{53}$ cm^{-3}. The excess flare light curve (cf. Fig. 2) is well fitted by an exponential function with an 1/e decay time $\tau_{\rm d}$ = 10000 s. The flare temperature (i.e. the 1-T results in Table 1) may also be described by an exponential decay with decay time $\tau_{\rm T} \simeq 23000$ s. The resulting (exponential) decay time for the thermal energy is $\tau_{\rm eff} \approx 11400$ s.

Subsituting $T_{\rm FL1}$, $EM_{\rm FL1}$ and $\tau_{\rm eff}$ in the above expressions gives the loop height H as a function of $N\alpha_{0.1}^2$ ($\alpha_{0.1} = \alpha/0.1$) as indicated in Fig. 9. The thick solid line is for a constant cross-section loop Γ = 1 and the thick dashed curve for a slightly

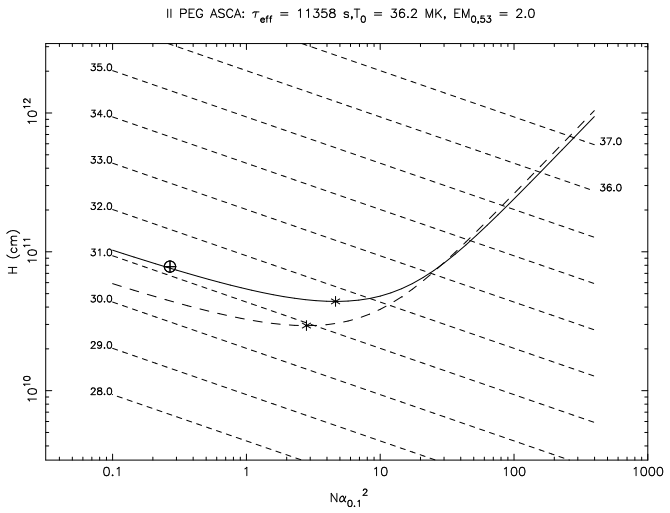

Fig. 9. Height H of the flare loop(s) as a function of the number of flaring loops N times the aspect ratio α squared. The aspect ratio is normalized to a value of 0.1 which is typically for solar loops. The thick solid line is for a rigid flux tube (Γ = 1) and the thick dashed one for a loop with an expanding cross section (Γ = 10). A temperature of 36 MK, an emission measure of 2 10^{53} cm^{-3} and an effective decay time of 11358 s were assumed. The grid of dashed lines are lines of constant volume. The values of log V(cm^3) are indicated by the labels. The $\oplus$ symbol indicates the solution of the quasi-static cooling model.

expanding loop Γ = 10. The grid of (thin) dashed lines indicate lines of constant volume. Along the Γ = 1 and the Γ = 10 curves the ratio of the radiative and the conductive cooling time $\tau_{\rm r}/\tau_{\rm c}$ changes. At the asterisks $\tau_{\rm r} = \tau_{\rm c}$ while to the left of the asterisks the radiative losses become increasingly important. For a single loop flare (N = 1) or a flare occuring in a few loops simultanuously ($N \approx 2-4$) the radiative losses are slightly more important than the conductive losses. The solid and dashed curves are reasonably flat in that range and can be used to derive a range of acceptable values of the loop height. The volume is however less constrained and can vary by a factor ten. Because $n_e \sim 1/\sqrt{V}$ the uncertainty in the derived value of the electron density is only a factor three.

The general problem encountered when deriving flare parameters from an observed decay is that the ratio $\tau_{\rm r}/\tau_{\rm c}$ is unknown and, even worse, may change during the decay of a flare. An exception to this is when the flare volume cools quasi-statically, that is, evolves through a sequence of quasi-static equilibria. At each instant a flare loop then satisfies the scaling laws for coronal loops but with a slowly varying effective heating. A description of the model can be found in VM89 (Sect. 3.2) and in Mewe et al. 1989. The quasi-static cooling model has been applied to several flares (Hünsch and Reimers, 1995, Ottmann and Schmitt, 1996). An advantage of the model is that it is easy to check whether it is applicable to a particular observation: because in the model $\tau_{\rm r}/\tau_{\rm c}$ is constant, also the ratio $T_7^{13/4}/EM_{53}$ should be constant. For the time intervals FL1, FL2 and FL3 we have that $T_7^{13/4}/EM_{53} = 33 \pm 6, 26 \pm 10, 38 \pm 15$ respectively. Although these values are not inconsistent with a constant value of $\tau_{\rm r}/\tau_{\rm c}$, they are not very convincing because of the large error bars.

In general however there is a problem with a straightforward application of the quasi-static model, or any other model, when only a few determinations of T and EM are available during the decay phase of a flare. During the decay phase both T and EM decrease as a function of time. If the exposures are very long, e.g. to get sufficient S/N, the resulting spectra can be considered as the sum of many isothermal spectra of varying strength (emission measure). If one fits such a spectrum the resulting temperature and emission measure are some ill-defined averages of the actual values of $T(t)$ and $EM(t)$ during the exposure. At different times during the exposure the instantaneous spectrum will contribute relatively more or less to the observed spectrum, depending on the actual magnitude of the intantaneous spectrum and the bandpass of the instrument. So for a time-dependent plasma there can be a discrepancy between the measured values of T and EM and the actual values. For shorter exposure times the values determined for T and EM of course approach the actual values. It is not surprising that for a cooling plasma sometimes a two-temperature fit gives as good results as a one temperature fit. Especially when the S/N is not excellent many decompositions of the observed spectrum into isothermal spectra are possible. Because we have only three measurements in the decay phase we can not fit the temperatures and emission measures directly with the model because the model describes the instantaneous values of T and EM. A safer approach is to consider the radiative losses which are proportional to $EM\Psi(T) \sim EMT^{1/4}$. The quasi-static cooling model predicts that (VM89, Table 5)

$$E_{\rm rad} \sim EM_0 T_0^{1/4} \left\{ 1 + \frac{t}{3\tau} \right\}^{-4} , \qquad (5)$$

with $\tau \equiv (3n_0kT_0)/(n_0^2\Psi_0T_0^{1/4})$ and EM_0 and T_0 the values of the emission measure and temperature at the start of the decay phase. For an exposure of duration Δt centered around time t, the average radiative losses during the exposure are given by

$$\overline{E}_{\rm rad} = \frac{1}{\Delta t} \int_{t-\Delta t/2}^{t+\Delta t/2} E_{\rm rad}(t')dt' . \qquad (6)$$

Substitution of Eq. (5) in this expression gives for the three intervals FL1 - FL3 three relations which can be fitted to the three values of $EMT^{1/4}$ as follow from Table 1. In this way we fit the observed time-averaged radiative losses to those predicted by the model. We note that a procedure consisting of fitting the time-averaged values of temperature and emission measure is unphysical.

The fitting was performed with $EM_0T_0^{1/4}$ and τ as free parameters resulting in $EM_{0,53}T_{0,7}^{1/4}$ = 2.72 and τ = 12950 s. We note that Eq. (5) is only valid when there is no additional heating during the decay. We checked for this possibility but found no significant improvement of the fit while the resulting values of τ are always in the range $12000-13500$ s. Using the value of τ and the scaling law it follows that V = 3 10^{31} cm^3,

Table 3. Comparison of physical flare parameters

	σ^2 CrB [1]	Algol[2]	II Peg[3]
$L_X(10^{30}$ erg/s)[4]	9.4	14	2.6
$E_{\rm tot}(10^{35}$ erg)[5]	0.24	1	0.27
$\tau_{\rm rise}$(s)	200	2000	$\lesssim$ 3000
$\tau_{\rm d}$(s)	1700	5600	10000
$\tau_{\rm T}$(s)	3200	11400	23000
$T_{\rm max}$(MK)	95	60	36
$EM(10^{53}$ cm$^{-3})$	5.6	9	2
$n_e(10^{11}$ cm$^{-3})$	9	2.6	0.8
$V(10^{30}$ cm$^3)$	0.7	14	30
$H(10^{10}$ cm)	1.4	5	8
B(G)	600	200	140

[1] van den Oord et al. 1988
[2] van den Oord and Mewe 1989
[3] $T_{\rm max}$ and EM should be considered as lower limits and τ_T as an upper limit.
[4] 0.1-10 keV peak luminosity.
[5] 0.1-10 keV total radiative losses.

L = 2.5 10^{11} cm, H = 8 10^{10} cm = 0.4R_*, $N\alpha_{0.1}^2$ = 0.27 and n_0 = 8 10^{10} cm^{-3}. These values correspond to the $\oplus$ symbol in Fig. 9. In the case of quasi-static cooling $\tau_{\rm r}/\tau_{\rm c}$ = 0.18 for $T >$ 20 MK. The quasi-static cooling point is not exactly on the Γ = 1 curve which is not surprising because the latter curve is derived under the assumption of an exponential time dependence for all physical quantities. The foot point area of the flare volume is $A = V/L$ = 1.3 10^{20} cm^2. The values for H and V do in fact not depend very much on the assumption of quasi-static cooling. Fig. 9 shows that these values differ at most by a factor of two if one uses only the Γ = 1 curve to estimate these.

A comparison with other flares (see Table 3) shows that the flare observed with ASCA is rather special. It has a very long duration, a large associated volume and a relatively low density. All these properties are of course related in the sense that a low density makes the cooling time long and the required volume large. The minimum value for the magnetic field required to confine the plasma is 140 G. The large length we found is comparable to the value found for the flare on II Peg observed with GINGA L = 9.3 $10^{10}\alpha_{0.1}^{-2/3}$ cm (Doyle et al., 1992b).

Suppose that during the impulsive phase of the flare, which is not observed, the total flare energy $E_{\rm tot}$ resides in particle beams. The beams are stopped in the dense chromosphere and heat a total of N chromospheric particles to a coronal temperature T. Then $3NkT \approx E_{\rm tot}$. When the heated plasma fills the coronal (flare) volume through the process of chromospheric evaporation then the resulting average density in the coronal volume is $n = N/V$. For T = 36 MK and $E_{\rm tot} \approx$ 2.7 10^{34} erg we find that n = 6 10^{10} cm^{-3} which is in good agreement with the value found from the quasi-static cooling model. In this interpretation the abundances found during the flare will reflect the chromospheric abundances. Ottmann and Schmitt (1996) have suggested chromospheric evaporation as a cause for the increase of the metal abundance detected during a flare on Algol.

For deriving the flare parameters we used a general cooling model and the quasi-static cooling model. Both models give reasonably consistent results. We note that the quasi-static cooling model predicts a distinct shape of the DEM. In VM89 this aspect was not considered because at that time the spectral resolution offered by EXOSAT did not allow for a DEM analyses. In the Appendix we derive the DEM distributions of quasi-statically cooling loops. We show that during a large part of the decay phase the DEM is insensitive to the presence of additional heating which explains why we found that our fits are insensitive to the assumed additional heating. We have tried to compare a DEM distribution for the whole decay phase (FL1 - FL3), with the DEM distributions given in the Appendix. The result is not conclusive because the coverage of the decay phase is not continuous, the flare spectra are noisy and the spectral resolution offered by ASCA is not high enough. For future missions, with higher spectral resolution, the DEM distributions discussed in the Appendix can be used as diagnostic tools for quasi-static cooling.

6. Discussion

6.1. Quiescent corona

For both EUVE and ASCA observations made at different times the application of various multi-temperature and DEM fitting techniques yields for the quiescent corona of II Peg a bimodal temperature structure with components 4 and 10 MK for the EUVE data and 10 and 20 MK for the ASCA data with all emission measures in the range $\sim$ 1-2 10^{53} cm^{-3}. These values are in agreement with the values obtained with GINGA. The power-law DEM distribution derived by Doyle et al. (1989b) corresponds to an emission measure of the plasma at temperatures between T_1 and T_2 of $EM(T_1,T_2)$ = 1.1 $10^{53}(1/\sqrt{T_{2,7}} - 1/\sqrt{T_{1,7}})$ where the temperatures are in units of 10 MK. The presence of very hot plasma ($T > 10^8$ K) in the corona of II Peg cannot be confirmed. Occasionally we found evidence for a very hot plasma component (cf. Fig. 8) but this is mainly caused by the hard flux above 7 keV. At these energies uncertainties in the instrumental calibration may play a role implying that ASCA data cannot be used to confirm the GINGA results.

6.1.1. Non-solar abundances?

An important result is that non-solar abundances are required to model the ASCA spectrum satisfactorily. But also for the modeling of the EUVE spectrum we certainly need a very low Fe abundance. The element with the best constrained abundance, i.e., iron, is underabundant by a factor of even 6-10 relative to solar photospheric (both for EUVE and ASCA spectra), while other elements (constrained by ASCA, i.e. O, Ne, Mg, Si, S, Ar, Ca, Ni) are underabundant by a factor 2-5. Especially, the very low Fe abundance is at variance with the "FIP" effect which pre-

dicts e.g., for Fe with its relatively low First Ionization Potential in the solar corona an *overabundance* by a factor of $\sim$ 3-5 with respect to solar photospheric values. The analyses of ASCA and EUVE spectra of other active stars such as RS CVn's, Algol-type binaries, and pre-main-sequence stars show a similar behaviour (e.g., reviews by White 1996 and Pallavicini et al. 1996). In addition to the assumption of true metal depletion which is still controversial, competing explanations for the EUVE results suggest that either the lines may be reduced by resonant scattering (Schrijver et al. 1994, 1995) or the apparent continuum level may be enhanced by a forest of weak unresolved lines missing in the current plasma codes. Though these effects may play a role in the formation of EUVE spectra, neither effect is expected to play a role in the ASCA spectra.

6.2. Flaring corona

In both sets of observations also a flare was detected. The flare in the EUVE observations was interpreted as an enhancement both in temperature ($\sim 2\times$) and emission measure ($\sim 4\times$) of the hot quiescent component and it appears that the flare has occurred in nearly all the hot quiescent-component region. The X-ray flare detected by ASCA has a peak temperature of at least 35 MK. Both flares have peak X-ray luminosities L_X(0.1-10.0 keV) a few times 10^{30} erg/s. These values are much higher than those measured in compact and two-ribbon flares on the Sun, generally higher than for flares on M dwarf flare stars (e.g., Pallavicini et al. 1990) and comparable to flares in RS CVn- and Algol-type systems (e.g., VMB88 and VM89).

6.2.1. Abundance variations in the flare

The X-ray flare detected by ASCA shows evidence for abundance variations. As it is known that abundances can vary during flares since Sylwester et al. (1984) detected for the first time metal (i.e. Ca) abundance variations in solar flares from high-resolution X-ray spectra we have investigated whether this could be the case in the flare detected by ASCA.

As a result we found that the metal (iron) abundance shows an enhancement of a factor of 4 compared to the quiescent value during the rise of the flare. In the later phases of the flare the metal abundance becomes equal to the corresponding quiescent value within the statistical uncertainty. This behaviour is similar to that observed e.g., in flares on AB Dor by ASCA (metal abundance rose from 0.3 to 0.8 during the rise and decreased to 0.5 during the decay) (White et al. 1996) and in a flare on Algol observed by ROSAT (increase from 0.2 to 0.8 during rise and decrease to 0.4 during decay) (Ottmann and Schmitt 1996). The latter authors suggest that the different chemical composition of the flaring corona that resembles more the photospheric one should be indicative of a chromospheric evaporation process. After heating by the flare the chromospheric material expands into the corona and would be responsible for the metal enrichment *if* this material has a relatively larger, i.e. more solar-photospheric like abundance. We have tested this hypothesis by fitting the FL1 spectrum with a "mixing" model consisting of two components: a coronal component (c) with abundances from Table 2 mixed with a photospheric component (ph) with solar photospheric abundances and the same temperature but different emission measure. As a result we obtained χ^2=151 (127 dof), a temperature 35.7 MK, a total emission measure 1.91 10^{53} cm^{-3} (i.e. values consistent with those given in Table 1), and a mixing ratio $EM_c : EM_{ph}$ = 2 : 1. This gives a value of the iron abundance (0.39) also consistent with that given in Table 1, while the resulting values for the other abundances (e.g., 0.45 for Si, 0.42 for Mg, etc.) are different from the values in Table 2 but within the statistical uncertainties.

6.2.2. Flare classification

How should we classify the flare on II Peg observed by ASCA? VM89 argue that the classification - compact (single-loop) flare $vs.$ 2-ribbon flare - should be based on the rise time rather than the decay time. The rise time of the Algol flare of about half an hour (cf. Table 3) is compatible with the filament rise time of a 2-ribbon flare which should classify this event as a 2-ribbon flare (VM89), whereas the much faster rise time of 3 min. classifies the flare on σ^2 CrB as a compact single-loop flare (VMB88).

Unfortunately, the flare on II Peg rose just during an Earth-blocking period of the ASCA observations so that the precise value of the rise time is not known. A comparison of the flare parameters (cf. Table 3) shows that the length, volume, and decay time are more similar to those for the flare on Algol than those for σ^2 CrB .

During solar two-ribbon flares the energy release can continue well into the decay phase of the flare. However, in Sect. 5 we found no convincing evidence for additional heating during the decay phase. There are two possible explanations for reconciling the solar and the II Peg observations. It is possible that during the decay phase of the flare we observed those loops which have formed by magnetic reconnection, contain a substantial amount of hot, evaporated plasma, and cool without any additional heating. The reconnection process still creates new, and larger, loops that do not contribute much to the observed emission. Secondly, Fig. 10 shows that during a large part of the decay phase, the differential emission measure distribution is insensitive to the presence of additional heating: the DEM curves for loop cooling with and without additional heating overlap for $T/T_0 \gtrsim 0.5$.

6.3. Alternative explanation for the abundances

Recently it was pointed out by van den Oord and Mewe (1996) that the effect of under-abundances of metals in stellar coronae can be simply the consequence of hydrostatic equilibrium. If a coronal loop is in hydrostatic equilibrium the scale heights of the individual ions can differ strongly from the mean scale height of the plasma. In this case a weak electrostatic field is present which couples the ion and electron fluids (Spitzer1962). Each ion has its own scale height determined by its charge and mass, due to the balance between the electric force and gravitation. As a result the ion distribution in a loop becomes in-

homogeneous and the line-to-continuum ratio depends on the scale height of the specific ion that emits a given spectral line. The resulting reduction of the line-to-continuum ratio can be interpreted as an under-abundance of metals in the corona. The derived abundances depend on the ions which emit the spectral lines and lines from different ions of the same element will result in (slightly) different abundances. With global spectral fitting techniques, the derived abundances are some weighted averages, depending on which lines are present in the spectrum. Under hydrostatic equilibrium reductions of the coronal metal abundances, when compared to photospheric abundances, by factors 2 - 10 can easily result. When during a flare chromospheric evaporation creates strong plasma flows in loops the ion stratification, which existed under hydrostatic equilibrium, disappears and the line-to-continuum ratio will indicate an increase of the metal abundances.

The settling of the ions to their (hydrostatic) equilibrium positions occurs through the process of element diffusion which is very slow in a dense loop but can be much faster (i.e. on a time scale of a few hours) in long loops with low densities. In the flaring structure as observed on II Peg with a height $H = 8\ 10^{10}$ cm the draining of the plasma during flare decay (reflected by the decrease of the emission measure) can be accompanied by a gravitational settling of the ions (reflected by the observed abundance decrease).

Acknowledgements. The Space Research Organization of the Netherlands (SRON) is supported financially by NWO, the Netherlands Organization for Scientific Research. G. van den Oord acknowledges financial support from NWO. We thank the referee Dr. J.G. Doyle for constructive remarks.

Appendix A: DEM-distribution of a quasi-statically cooling loop

In Sect. 5 we argued that an application of the quasi-static cooling model requires that during the decay of the flare as many temperature and emission measure determinations as possible are obtained. Shorter integration times imply that the thus obtained values for T and EM represent the actual values instead of some ill-defined averages. On the other hand, shorter integration times result in a reduction of the S/N. This problem can be circumvented when an exposure of the complete decay phase is obtained and the resulting spectrum has a moderate to high spectral resolution. In that case a differential emission measure analyses can be made and the resulting DEM can be compared with the theoretical prediction by the quasi-static cooling model. In this Appendix we derive the DEM-distribution of a quasi-statically cooling loop. The basic equations of the quasi-static cooling model are (see VM89)

$$\frac{dT}{dt} = \frac{8}{21\tau}\frac{T_{\rm e}^{7/2} - T^{7/2}}{T_0^{7/8} T^{13/8}}\ , \tag{A1}$$

$$EM(t) = EM_0 \left(\frac{T}{T_0}\right)^{13/4} \tag{A2}$$

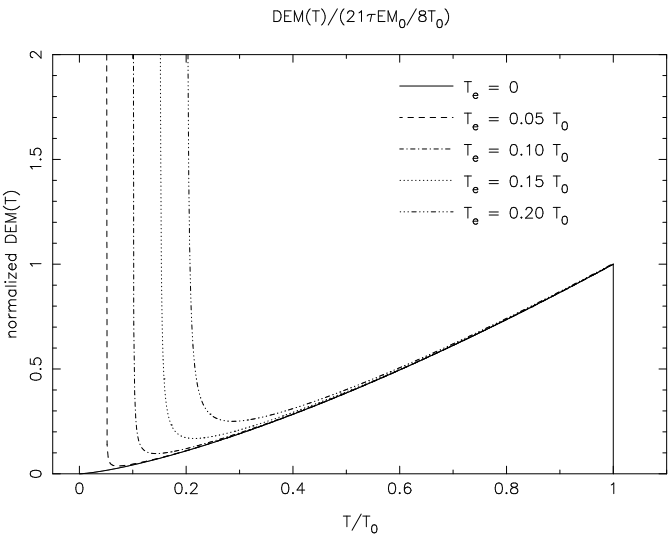

Fig. 10. DEM-distribution according to the quasi-static cooling model. $T_{\rm e}$ is the temperature reached at the end of the decay phase. When no additional heating is present $T_{\rm e} = 0$.

with index 0 indicating the start of the decay phase. $T_{\rm e}$ is the temperature reached at the end of the decay phase. When no additional heating is present during the decay phase $T_{\rm e} = 0$. The spectrum of an isothermal source at a given time t is given by

$$f(\lambda, t) = \int \Psi(\lambda, T(t)) n(t)^2 dV \tag{A3}$$

with λ the wavelength, $\Psi(\lambda, T)$ the emissivity and n the electron density. The average flux F received after an exposure of length Δt is

$$F(\lambda) = \frac{1}{\Delta t}\int_{t_i}^{t_i+\Delta t} \Psi(\lambda, T(t)) EM(t) dt\ . \tag{A4}$$

Using Eqs. (A1) and (A2) we can write

$$F = \frac{21}{8}\frac{\tau EM_0}{\Delta t}\times \int_{T(t_i+\Delta t)}^{T(t_i)} \Psi(\lambda, T(t)) \frac{T^{39/8}}{T_0^{19/8}(T^{7/2} - T_{\rm e}^{7/2})} dT\ . \tag{A5}$$

Using the formal definition of the DEM

$$F(\lambda) \equiv \frac{1}{\Delta t}\int_{T(t_i)}^{T(t_i+\Delta t)} \Psi(\lambda, T(t)) DEM(T) dT$$

and comparing this expression with Eq. (A5), we can make the following identification

$$DEM(T) = \frac{21}{8}\frac{\tau EM_0}{T_0}\frac{(T/T_0)^{39/8}}{(T/T_0)^{7/2} - (T_{\rm e}/T_0)^{7/2}} H(T_0 - T) \tag{A6}$$

where H is the Heaviside function. This expression shows that a quasi-statically cooling loop has a $DEM \sim T^{11/8}$ distribution

when no additional heating is present during the decay phase. When a logarithmic binning of the temperature is used in the differential emission measure analysis one has $EM \sim T^{19/8}$. In Fig. 10 we show the DEM distributions for various values of T_e. When a finite exposure time is used during the decay phase, only a part of the DEM distributions shown in the figure contribute to the spectrum. Additional heating becomes only important towards the end of the decay phase, so at the low-temperature end of the DEM-distribution. Exposures at the start of the decay phase will contain almost no information about additional heating.

References

Anders, E., Grevesse, N., 1989, Geochim. Cosmochim. Acta 53, 197
Andrews, A.D., Rodonò, M., Linsky, J.L. et al., 1988, A&A 204, 177
Arnaud, M., Raymond, J., 1992, ApJ 398, 394
Arnaud, M., Rothenflug, R., 1985, A&AS 60, 425
Byrne, P.B., Lanzafame, A.C., Sarro, L.M., Ryans, R., 1994, MNRAS 270, 427
Byrne, P.B., Panagi, P.M., Doyle, J.G. et al., 1989, A&A 214, 227
Byrne, P.B., Panagi, P.M., Lanzafame, A.C. et al., 1995, A&A 115, 115
Dowdy Jr., J.F., Moore, R.L., Wu, S.T., 1985, Sol. Phys. 99, 79
Doyle, J.G., Butler, C.J., Byrne, P.B. et al., 1989a, A&A 223, 219
Doyle, J.G., Byrne, P.B., van den Oord, G.H.J., 1989b, A&A 224, 153
Doyle, J.G., Kellett, B.J., Butler, C.J. et al., 1992a, A&AS 96, 351
Doyle, J.G., van den Oord, G.H.J., Kellett, B.J., 1992b, A&A 262, 533
Feldman, U., Mandelbaum, P., Seely, J.F. et al., 1994, ApJ 421, 843
Golub, L., Maxson, C., Rosner, R. et al. 1980, ApJ 238, 343
Hünsch, M., Reimers, D., 1995, A&A 296, 509
Jenkins, L.F., 1963, General Catalogue of Trigonometric Parallaxes (New Haven: Yale University Observatory)
Kaastra, J.S., Mewe, R., 1993, Legacy 3, 16
Kaastra, J.S., Mewe, R., Nieuwenhuijzen, H., 1996a, in: Yamashita, K., Watanabe, T. (eds.), UV and X-ray Spectroscopy of Astrophysical and Laboratory Plasmas, Universal Academy Press, Inc., Tokyo, p. 411
Kaastra, J.S., Mewe, R., Liedahl, D.A. et al., 1996b, A&A 314, 547
Lemen, J.R., Mewe, R., Schrijver, C.J., Fludra, A., 1989, ApJ 341, 474
Liedahl, D.A., Osterheld, A.L., Goldstein, W.H., 1995, ApJ 438, L115
Mathoudiakis, M., Doyle, J.G., Avgoloupis, S. et al., 1992, MNRAS 255, 48
Mewe, R., Gronenschild, E.H.B.M., van den Oord, G.H.J., 1985, A&A Suppl, 62 197
Mewe, R., Kaastra, J.S., Liedahl, D.A., 1995, Legacy 6, 16
Mewe, R., Kaastra, J.S., White, S.M., Pallavicini, R., 1996, A&A 315, 170
Mewe, R., Lemen, J.R., van den Oord, G.H.J., 1986, A&A Suppl 65, 511
Mewe, R., van den Oord, G.H.J., Jakimiec, J., 1989, in: Haisch, B.M., Rodonò, M. (eds.), Solar and Stellar Flares, IAU Coll. 104, Poster Papers, Catania Observatory Special Publ., p. 123
Morrison, R., McCammon, D., 1983, ApJ 270, 119
Ottmann, R., Schmitt, J.H.M.M., 1996, A&A 307, 813
Pallavicini, R., Tagliaferri, G., Stella, L., 1990, A&A 228, 403
Pallavicini, R., White, N.E., Mewe, R., 1996, A&A Review, in press
Paresce, F., 1984, AJ 89, 1022
Patterer, R.J., Vedder, P.W., Jelinsky, P. et al., 1993, ApJ 414, L57
Rodonò, M., Byrne, P.B., Neff, J.E. et al., 1987, A&A 176, 267
Rodonò, M., Cutispoto, G., Pazzani, V. et al., 1986, A&A 165, 135
Rucinski, S.M., 1977, PASP 89, 280
Rumph, T., Bowyer, S., Vennes, S, 1994, AJ 107, 2108
Schrijver, C.J., van den Oord, G.H.J., Mewe, R., 1994, A&A 289, L23
Schrijver, C.J., van den Oord, G.H.J., Mewe, R., Kaastra, J.S., 1995, A&A 302, 438
Spitzer, L., 1962, Physics of fully ionized gases, Interscience, NY
Swank, J.H., White, N.E., Holt, S.S., Becker, R.H., 1981, ApJ, 246, 208
Strassmeier, K.G., et al., 1988, A&AS 72, 291
Sylwester, J., Lemen, J.R., Mewe, R., 1984, Nature 310, 665
Tagliaferri, G., White, N.E., Doyle, J.G. et al., 1991, A&A 251, 161
van den Oord, G.H.J., De Bruyn, A.G. 1994, A&A, 286, 181
van den Oord, G.H.J., Mewe, R., Brinkman, A.C., 1988, A&A 205, 181 (VMB88)
van den Oord, G.H.J., Mewe, R., 1989, A&A 213, 245 (VM89)
van den Oord, G.H.J., Mewe, R., 1996, A&A, submitted
Vogt, S.S., 1981, ApJ 247, 975
White, N.E., 1996, in: Pallavicini, R., Dupree, A.K. (eds.), Cool Stars, Stellar Systems, and the Sun, PASP Conf. Series, in press
White, S.M., Pallavicini, R., Lim, J., 1996, in: Gershberg, R., Griener, J., Duerbeck, H. (eds.), Flares and Flashes, in press

This article was processed by the author using Springer-Verlag LaTeX A&A style file *L-AA* version 3.